Semicond. Sci. Technol. **25** (2010) 034002 (7pp) doi:10.1088/0268-1242/25/3/034002

Energy and transport gaps in etched graphene nanoribbons

F Molitor, C Stampfer, J Güttinger, A Jacobsen, T Ihn and K Ensslin

Solid State Physics Laboratory, ETH Zurich, 8093 Zurich, Switzerland

E-mail: fmolitor@phys.ethz.ch and stampfer@phys.ethz.ch

Received 15 April 2009, in final form 30 May 2009
Published 3 February 2010
Online at stacks.iop.org/SST/25/034002

Abstract

We report transport measurements on etched graphene nanoribbons. We show that two distinct voltage (i.e. energy) scales can be experimentally extracted for characterizing the parameter regions of suppressed conductance at low charge density in graphene nanoribbons. The energy scales are related to the charging energy of localized states and to the strength of the disorder potential. We discuss the scaling behaviour of these two energy scales as a function of the minimum width w for a number of different devices. Finally, we present a model based on Coulomb blockade, due to quantum dots forming inside the nanoribbon, explaining the observed energy scales.

(Some figures in this article are in colour only in the electronic version)

1. Introduction

Graphene nanoribbons, in contrast to truly two-dimensional (2D) graphene [1], exhibit an effective energy gap, which overcomes the gapless band structure of graphene. Thus, graphene nanoribbons (including constrictions) show an overall semiconducting behaviour, which makes these quasi-1D graphene nanostructures promising candidates for the fabrication of nanoscale graphene transistors [2–4], tunnel barriers, quantum dots [5–9] and charge detectors [10]. On the other hand, ideal graphene nanoribbons [11–14] promise interesting quasi-1D physics with strong relations to single-walled carbon nanotubes [15, 16], including phenomena beyond nanotube physics, such as for example spin-polarized edge states [17, 18]. Transport through graphene nanoribbons has been studied by a number of groups [19–24], and transport and energy gaps are observed experimentally.

From a theoretical point of view, a number of theoretical predictions have been put forward to describe a (clean confinement) energy gap in graphene nanoribbons. Along these lines, zone-folding approximations [12], π-orbital tight binding models [25, 26], and first principle calculations [27, 28] predict an energy gap E_g scaling as $E_g(w) = \alpha/w$ with the nanoribbon width w, where α is in the range of 0.2–1.5 eV nm, depending on the model and the crystallographic orientation of the graphene nanoribbon [29]. However, these theoretical estimates can neither explain the experimentally observed energy or transport gaps of etched nanoribbons (with rough edges, see figure 1(*a*)) of widths beyond 20 nm, which turn out to be significantly larger than predicted, nor do they explain the large number of resonances experimentally found inside the transport gap [19–24]. This has led to the suggestion [30] that localized states (and interaction effects) due to edge roughness, disorder, such as bulk disorder, or bond contractions at the edges may dominate the transport gap. Several mechanisms have been proposed to describe the observed gap, including re-normalized lateral confinement [20], quasi-1D Anderson localization [31], percolation models [32] and many-body effects (incl. quantum dots) [33], where substantial edge roughness is required. It has also been shown that moderate amounts of edge roughness can substantially suppress the linear conductance near the charge neutrality point [34], giving rise to localized states relevant for both single-particle and many-body descriptions.

In this paper, we show experimental evidence that the transport gaps in etched graphene nanoribbons available so far (see figure 1) are, in contrast to the prediction of clean energy gaps, primarily formed by local resonances and quantum dots along the nanoribbons. In section 2, we start by reviewing the fabrication process used to make etched graphene nanoribbons. Transport measurements are presented in section 3, and in section 4, we discuss the dependence of the energy gaps on the nanoribbon's width w. Finally, we describe a model based on Coulomb blockade inside the nanoribbon, explaining the large number of reproducible

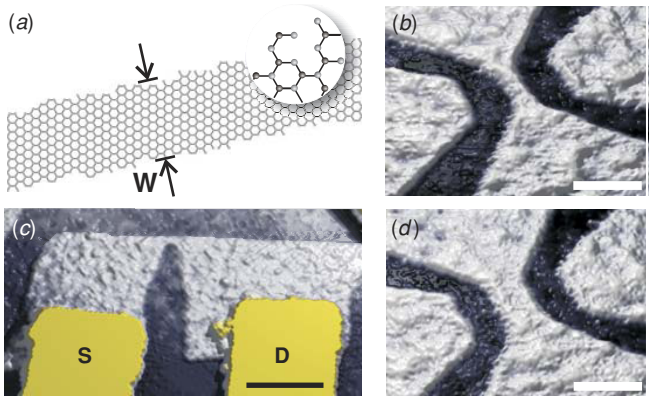

Figure 1. Schematic illustration of an etched graphene nanoribbon with rough edges and a width of $w \approx 2.3$ nm. The inset highlights the rough edges of the honeycomb lattice of graphene. (*b*) Scanning force microscope (SFM) image of a fabricated graphene nanoribbon with two side gates (see bright areas) resting on SiO_2 (dark areas). This nanoribbon has a width of $w \approx 30$ nm and a length of $w \approx 100$ nm. (*c*) SFM image of a narrow graphene constrictions after contacting the flake to source (S) and drain (D) lead. The Cr/Au contacts are highlighted in yellow. (*d*) SFM image similar to panel (*b*) of a different device with a typical width of $w \approx 65$ nm. The white scale bars in this figure correspond to 100 nm and the black bar corresponds to 500 nm.

conductance resonances and the scaling of the observed energy gaps.

2. Fabrication of graphene nanoribbons

The state-of-the-art fabrication process of graphene nanodevices, which has been mostly developed by Geim and Novoselov [35, 36] and by Kim and coworkers [37], is summarized in figure 2. The substrate material consists of highly doped silicon (Si^{++}) bulk material covered with approximately 300 nm of silicon oxide (SiO_2), where the thickness and roughness of the SiO_2 top layer are crucial for the identification and further processing of single-layer graphene samples (figure 2(*a*)). Before depositing graphene, standard photolithography followed by metallization (usually chrome/gold) and lift-off is used to pattern arrays of reference alignment markers on the substrate that are later used to re-identify locations (of individual graphene flakes) on the chip and to align further processing patterns including the metallic contacts connecting the flake (figures 2(*b*) and (*c*)). The deposition of graphene is based on mechanical exfoliation of (natural) graphite by adhesive tapes [35]. In 2005, two groups [36, 37] proved that this simple technique indeed leads to high-quality single-layer graphene flakes resting on the SiO_2 surface. After the exfoliation and deposition there are graphite flakes with all kinds of layer thicknesses on the sample. The main difficulty is to find the thinnest among them, i.e. the single-layer graphene. Surprisingly, an optical microscope in combination with a carefully selected oxide thickness is sufficient for locating individual graphene flakes. This technique is in wide use for the identification of graphene flakes since optical microscopy, in contrast to AFM and Raman imaging techniques, provides sufficient throughput for scanning large-area samples. However, an optical image cannot unambiguously distinguish between single- and bi-layer graphene. Therefore, Raman spectroscopy [38–40] and AFM techniques are indispensable tools for fully characterizing graphene flakes. Next the graphene flake has to be structured to submicron dimensions in order to fulfil the device design requirements. The commonly used technique is based on resist spin coating, electron beam lithography (EBL), development and subsequent etching of the unprotected graphene. This processing sequence is illustrated in figures 2(*d*)–(*f*). The resist (polymethylmetha crylat (PMMA)) has a thickness that varies between 50 and 100 nm. This limits on one hand the minimum feature size of the final graphene devices and on the other hand the process window for the actual etching step. It has been found that short (5–15 s) mainly physical reactive ion etching (RIE) based on argon and oxygen (80/20) provides good results without influencing the overall quality of the graphene flake [41]. With reactive ion etching, the chemical bonds of the etch target are broken up by physical bombardment with argon ions which were created in a plasma. On the bombarded sites, chemical etching (in our case with oxygen) can be enhanced by the heightened chemical reactiveness of the etchant species due to the plasma. Hence this process combines the anisotropic etching possibilities of the physical bombardment, with the material selectivity of the chemical etching. The ability of this process to etch up to around five-layer-thick flakes facilitates contacting structures because it reduces the risk of short contacts due to thicker graphitic regions. After etching and removing the residual EBL resist, scanning force microscope images (as shown e.g. in figures 1(*b*) and (*d*)) are of importance to prove the quality of the patterned graphene flakes mainly in terms of surface contamination. Here the step height and the surface roughness of the flake, which should be lower than 0.2 nm rms, are good quality measures for flakes before contacting. Selected graphene (nano)structures are then contacted by an additional EBL step, followed by metallization and lift-off, as illustrated in figures 2(*f*)–(*h*). Two layers of EBL resist are used to provide a T-shaped resist profile allowing us to pattern metal structures down to a lateral size of around 70 nm. After development 2–5 nm chrome (Cr) or titanium (Ti) and 30–50 nm gold (Au) are evaporated for contacting the preselected graphene nanostructures. In figure 1(*c*), we show an SFM image of a contacted graphene nanostructure after a successful lift-off process. This image also proves the alignment between the graphene nanostructure and the metal electrodes to be sufficiently good. The graphene sample is now ready for wire bonding in a chip carrier, which is generally a crucial step for transport studies on nanodevices.

3. Energy gaps in etched graphene nanoribbbons

The graphene nanoribbon devices (examples shown in figures 1(*b*)–(*d*)) are measured in two-terminal (source (S) and drain (D), see figure 1(*c*)) geometry by low-frequency lock-in techniques either in a cryostat with a variable temperature insert at $T \approx 1.7$ K, or in a dilution refrigerator at an electron temperature of $T \approx 200$ mK. In figure 3(*a*), we show an

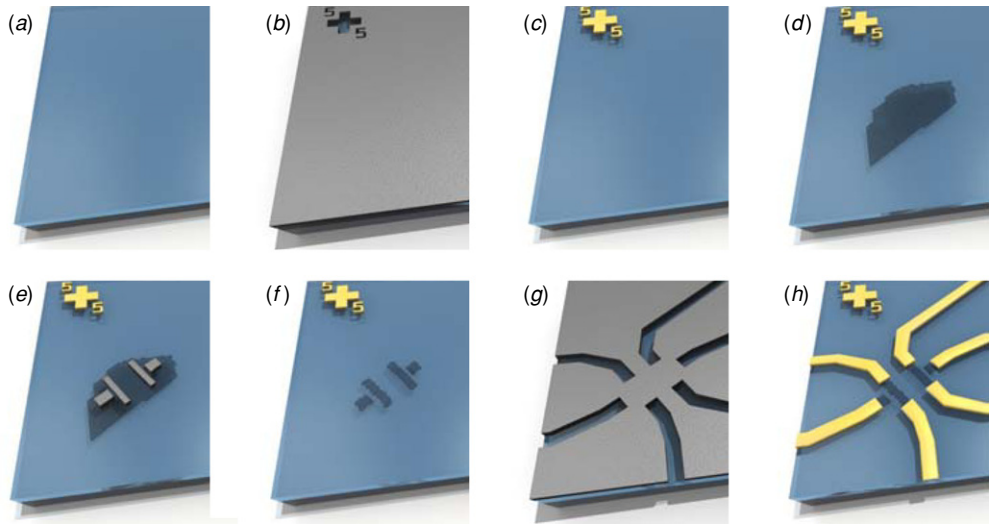

Figure 2. Fabrication process. (*a*) Starting point is a silicon substrate with a 290 nm thick silicon dioxide on top. (*b*) With optical lithography orientation numbers for the flakes and markers used for the alignment during the subsequent electron beam lithography (EBL) steps are patterned into the photo resist. (*c*) The structure is then made with evaporation of chromium and gold, followed by a lift-off process. (*d*) Deposition of graphene on the substrate and identification of single-layer flakes using an optical microscope and Raman spectroscopy. (*e*) and (*f*) Patterning of the flakes by EBL and etching by reactive ion etch (RIE). (*g*) An additional EBL step is performed for defining the contacts, which are then made by evaporation of chromium and gold, followed by a lift-off process. (*h*) Final device, ready for bonding.

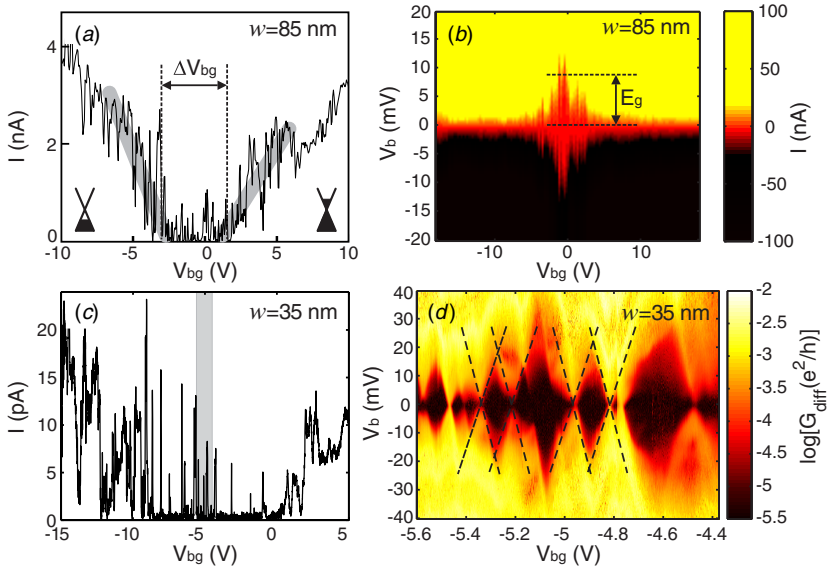

Figure 3. Transport gap measurements on two different graphene nanoribbons. (*a*) Back-gate characteristics at low bias ($V_b = 300\ \mu$V) for a nanoribbon with dimensions $w = 85$ nm, $l = 500$ nm. Transport can be tuned from being hole (left inset) to electron dominated (right inset) and the gap in the back gate $\Delta V_{\rm bg}$ is highlighted (*b*) Corresponding color plot of the source–drain current as a function of the applied back gate and bias voltage for the same device. The energy gap in bias direction E_g is highlighted. (*c*) BG characteristic (again $V_b = 300\ \mu$V) measured on a significantly smaller nanoribbon exhibiting a larger $\Delta V_{\rm bg}$, with pronounced resonances inside the transport gap. (*d*) Corresponding diamond measurements, i.e. conductance measurements as a function of bias and back-gate voltage. The measurements have been taken in a narrow back-gate range, see the highlighted area in panel (*c*).

example of the low bias ($V_b = 300\ \mu\text{V} \ll 4k_BT$) back-gate-dependent conductance of a nanoribbon with (minimum) width $w = 85$ nm and length $l = 500$ nm. Here we tune transport from the hole regime (lower-left inset) to the electron regime (lower-right inset). The region $-3V < V_{\rm bg} < 2V$ of suppressed conductance (indicated by the arrow labelled $\Delta V_{\rm bg}$) is the so-called transport gap in the BG voltage ($\Delta V_{\rm bg} \approx 5$ V). In contrast to the energy gap predicted for samples without disorder, where transport is completely pinched-off, we observe - in good agreement with other experimental work [1, 2, 8] - a large number of reproducible conductance resonances inside the gap. It has been shown that the broadening of some of these resonance peaks inside the transport gap is limited by temperature rather than by the lifetime of the resonance [22]. These resonances are even more pronounced on narrower nanoribbons, as shown in figure 3(*c*), where we plot the low bias back-gate-dependent conductance of a short and narrow $w \approx 35$ nm nanoribbon

(SFM shown in figure 1(*c*)) exhibiting a transport gap of the order of $\Delta V_{\rm bg} \approx 10$ V.

In figure 3(*b*), we show a source–drain current measurement of the $w = 85$ nm nanoribbon as a function of the source–drain bias V_b and back-gate voltage $V_{\rm bg}$ (i.e. Fermi energy). Here, regions of strongly suppressed current (red or grey areas) are observed, leading to an effective energy gap in the bias direction inside the transport gap in back-gate voltage (shown in figure 3(*a*)). Highly nonlinear *I*–*V* traces (not shown) are characteristic for the energy gap in the source–drain bias voltage direction. Moreover, we observe strong fluctuations (i.e. fringes) in the outline of the suppressed current region, which provides strong indications for the presence of local resonances. Overall, this energy gap agrees reasonably well with the observations reported in [20, 33], where an energy gap of $E_g = 10$ meV, for $w = 85$ nm, is found (see also below). In figure 3(*d*), we show an example of a high-resolution differential conductance $\mathrm{d}I/\mathrm{d}V_b$ measurement taken on the narrower ribbon ($w \approx 35$ nm) in a significantly smaller BG voltage range (see the marked region in figure 3(*c*)). At this scale, transport is dominated by well distinguishable, but sometimes intersecting diamonds of suppressed conductance (see the dark areas and dashed lines in figure 3(*d*)), which indicates that transport is blocked by localized electronic states or quantum dots (see also [21, 22]).

The transport gap in source–drain bias voltage, which is related to the energy gap E_g, and the transport gap $\Delta V_{\rm bg}$ in back-gate voltage are two distinct voltage scales resulting from the experiment. The quantity $\Delta V_{\rm bg}$ is measured at constant (nearly zero transport window) V_b but varying Fermi energy $E_{\rm F}$. Varying the magnitude of the transport window V_b at fixed Fermi energy gives rise to the transport gap in source–drain bias voltage. However, an explicit quantification of both voltage scales is rather challenging.

3.1. Transport gap in back gate

One way of quantifying the size of the transport gap in the back-gate voltage $\Delta V_{\rm bg}$ is illustrated in figure 3(*a*) and discussed in detail in [23]. The conductance trace is smoothened over a back-gate voltage range, large enough to eliminate the (reproducible) resonances without affecting the general shape of the back-gate trace. The regions of a linear increase of the conductance at both sides of the transport gap are selected (by hand), and a linear fit is performed (see grey bold lines in figure 3(*a*)). The gap size in the back-gate voltage $\Delta V_{\rm bg}$ is then defined as the distance between the intersection points of the fitted traces with the $I = 0$ line (here, $\Delta V_{\rm bg} = 5$ V). This is a reasonable approach since the conductance values are much smaller than the minimal conductivity observed for extended graphene systems which are of the order of $4\,\mathrm{e}^2/h$ [23]. Also different approaches to define the gap have been applied, as for example by defining a cutoff current. However, the overall results are the same, even if the details change slightly [23].

The corresponding energy scale $\Delta E_{\rm F}$ related to $\Delta V_{\rm bg}$ can be estimated from $\Delta E_{\rm F} \approx \hbar v_{\rm F}\sqrt{(2C_g \Delta V_{\rm bg}/|e|}$, where C_g is the back-gate capacitance per area [22] and $v_{\rm F} = 10^6$ m s^{-1} is the Fermi velocity of charge carriers. For the measurements shown in figure 3(*a*) we find, for example, an energy gap $\Delta E_{\rm F} \approx 100{-}310$ meV which is more than one order of magnitude larger than $E_g = 10$ meV (see figure 3(*b*)). This discrepancy has been attributed to different physical situations described by these two energy scales [21, 22], which will be further elucidated below.

3.2. Energy gap in the bias direction

More insight into the physics of the energy gap in the bias direction E_g (figure 3(*b*)) can be gained by focusing on a smaller back-gate voltage range as shown, e.g. in figure 3(*d*) which is a high-resolution close-up of the differential conductance $G_{\rm diff} = \mathrm{d}I/\mathrm{d}V_b$ of a plot similar to that shown in figure 3(*b*). Transport is dominated by diamonds of suppressed conductance, indicating that transport is blocked by localized states or quantum dots [21, 22]. The charging energy E_c, which is related to the quantum dot size, depends not only on the Fermi energy in a small back-gate voltage range (see e.g. different diamond sizes in figure 3(*d*)), but also on a large scale (e.g. [22]). It has been shown that the outline of figure 3(*b*) can indeed be obtained by plotting individually extracted charging energies as a function of $V_{\rm bg}$ over a large back-gate voltage range [22]. In the following, the energy gap in the bias direction E_g will be defined as the maximum charging energy $E_{c,\max}$, which is directly related to the smallest charged island along the nanoribbon ever forming when the density is swept.

4. Coulomb blockade in graphene nanoribbons

The experimental data shown above provide indications that the two experimentally observed energy scales E_g and $\Delta E_{\rm F}$ (i.e. $\Delta V_{\rm bg}$) are related to charged islands or quantum dots forming (spontaneously) along the nanoribbon. Similar observations were reported in [21, 22, 24]. This is supported by the observation of (i) Coulomb diamonds, which vary in size as a function of the Fermi energy (figure 3(*d*)), (ii) a variation of the relative lever arms of individual resonances [22], (iii) the detection of individual charging events inside the ribbon (figure 3(*d*)) [21–23], and (iv) an energy gap–width dependence well described by $E_g(w) = \alpha/w\,\mathrm{e}^{-\beta w}$ (see also below) [33]. Quantum dots along the nanoribbon can arise in the presence of a quantum confinement energy gap ($\Delta E_{\rm con}$) combined with a strong bulk and/or edge-induced disorder potential $\Delta_{\rm dis}$, as illustrated in figure 4(*b*). The confinement energy can be estimated by $\Delta E_{\rm con}(w) = \gamma\pi a_{C-C}/w$, where $\gamma \approx 2.7$ eV and $a_{C-C} = 0.142$ nm [12]. This leads, for example, to $\Delta E_{\rm con} = 26$ meV for $w = 45$ nm, which by itself can neither explain the observed energy scale $\Delta E_{\rm F} \approx$ 110–340 meV [22] nor the formation of quantum dots in the nanoribbon. However, by superimposing a disorder potential giving rise to electron–hole puddles near the charge neutrality point (see figure 4(*a*)) [42], the confinement gap ensures that Klein tunnelling (from puddle to puddle) present in the two-dimensional graphene is absent in nanoribbons, and conventional interband tunnelling takes over (figure 4(*b*)).

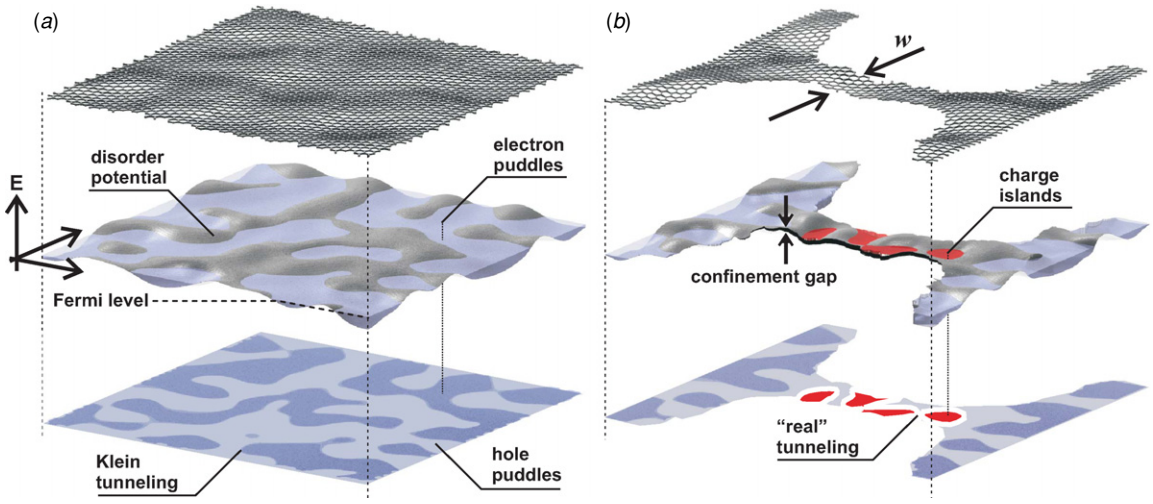

Figure 4. Schematic illustration summarizing the mechanism behind the formation of charged islands and quantum dots in graphene nanoribbons. (*a*) Two-dimensional graphene (as illustrated on the very top). A disorder potential (arising from both intrinsic and extrinsic effects) leads to the formation of electron and hole puddles in the near vicinity of the charge neutrality point (thus, at low-carrier densities). Since graphene has no band gap and carriers mimic relativistic particles Klein tunnelling and related phenomena make the boundary between electron and hole puddles reasonably transparent. (*b*) Graphene nanoribbon etched out of the original flake (see very top). The finite width w introduces a confinement gap (see the black line in the central panel), which isolates individual charge islands or quantum dots. Due to the confinement gap Klein tunnelling gets substituted by "real" tunneling as highlighted by the lower panel.

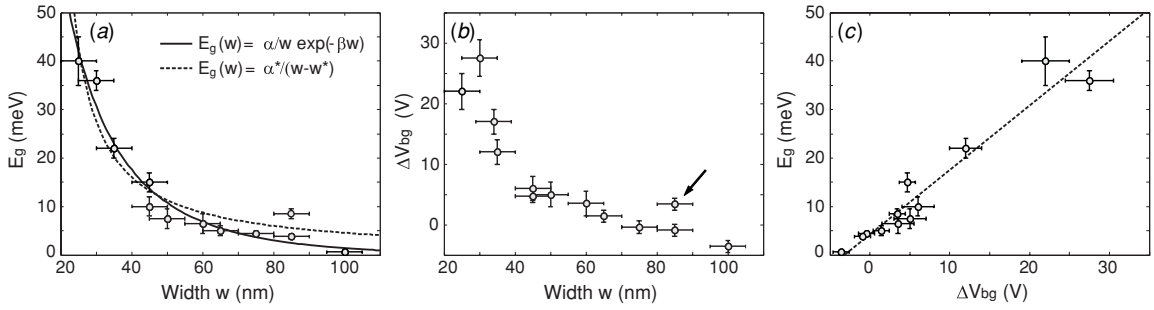

Figure 5. (*a*) Energy gap E_g as function of (minimum width) width w for 12 different graphene nanoribbon and nanoribbon-like devices. The experimental data can be well described by two-parameter models as shown by the solid and dashed lines. For more information please see the text. (*b*) The corresponding transport gap in the back-gate voltage $\Delta V_{\rm bg}$ as a function of width, where a very similar trend is observed as in panel (*a*). This is emphasized in panel (*c*) where the almost linear relation between E_g and $\Delta V_{\rm bg}$ is shown. The dashed line is a linear fit to the data points.

Within this model, $\Delta E_{\rm F}$ depends on both the confinement energy gap and disorder potential. An upper bound for the magnitude of the disorder potential can be estimated from our data to be given by $\Delta E_{\rm F}$. Comparing to [42] where a bulk carrier density fluctuation of the order of $\Delta n \approx \pm 2 \times 10^{11}$ cm^{-2} was reported, we find reasonable agreement as the corresponding variation of the local potential is $\Delta E_{\rm F} \approx 126$ meV. Following [22], we can estimate the fraction of overlapping diamonds by summing over all charging energies E_c, which leads, e.g. to $\sum E_c \approx 630$ meV. Comparison with the estimate for $\Delta E_{\rm F}$ gives 45–82% overlapping diamonds. We expect that this value depends strongly on the length of the nanoribbon in agreement with the findings of [23]. The energy gap E_g in the bias direction does not tell much about the magnitude of the disorder potential, but it is rather related to the sizes of the charged islands. In particular, the minimum island size is related to the maximum charging energy $E_{c,\max}$. By using the disc–capacitor model, we can estimate the effective charged island diameter by $d = e^2/(4\epsilon\epsilon_r E_c) \approx 100$ nm (where $\epsilon_r = (1 + 4)/2$), which exceeds the nanoribbon width w. Thus, in ribbons of different width the charging energy will scale closely, with w giving the experimentally observed $1/w$ dependence of E_g, as shown in figure 5(*a*) and [20, 33, 23].

5. Scaling of energy gaps in nanoribbons

In figure 5(*a*), we summarize the energy gaps measured in the source–drain bias direction E_g (estimated as shown, e.g., in figure 3(*b*)) as a function of w for a number of different samples with different geometries, and different minimum width w and length l. The error bars in the horizontal direction result from the SFM scans, while the vertical error bars are determined from the scatter of the charging energies extracted from Coulomb blockade diamond measurements as shown above. We observe a decreasing energy gap E_g with increasing constriction width w, in good agreement with the

observations by Han *et al* [20]. Indeed, despite the different fabrication process (Han and colleagues use HSQ as the resist, and do not remove it prior to the measurements), we find good agreement also on a quantitative level. For example, we can fit our data in figure 5(*a*) by $E_g(w) = \alpha^*/(w - w^*)$, where $\alpha^* = 0.38$ eV nm and $w^* = 16$ nm account for inactive edges [20]. These values are in good agreement with those reported by Han *et al* [20] and moreover, we also observe the systematic overestimation of E_g for wider ($w > 60$ nm) graphene nanoribbons. Following Sols *et al* [33], the energy gap may be interpreted as the renormalized charging energy of strongly coupled quantum dots. In the frame of their model, we can fit the energy gap by $E_g(w) = \alpha/w\, e^{-\beta w}$ and find $\alpha = 2$ eV nm and $\beta = 0.026$ nm^{-1} (see the solid line in figure 5(*a*)), again in good agreement with [33].

In figure 5(*b*), we plot the corresponding transport gaps in the back-gate voltage ΔV_{bg} as a function of width w. We observe a very similar trend for ΔV_{bg} as that described in figure 5(*a*) for E_g. However, the value of ΔV_{bg} is offset by a constant which depends on the conductance (or current) value chosen to measure the distance between the fitted linear slopes (see figure 3(*a*) and [23]). With the choice of taking the intersection at $I = 0$, a negative value of ΔV_{bg} means that the intersection point of the two fitted linear lines lies at a positive conductance value. In these cases, even though the conductance is reduced due to localized states in the constriction, it is never completely suppressed [23]. For nanoribbons with different lengths but equal nominal width, we observe in both E_g and ΔV_{bg} a significant increase for increasing nanoribbon length. Since most of our nanoribbons are in the range below 100 nm in length, we find, for example, a systematic increase in E_g and ΔV_{bg} for a nanoribbon with $l = 500$ nm (and $w = 85$ nm), compared to a ribbon with the same width, but $l = 200$ nm, as highlighted by the arrow in figure 2(*b*). This can be understood in a percolation picture by realizing that increasing the length (or decreasing the width) decreases the probability of the existence of at least one percolating conductive path through the nanoribbon. In the picture of randomly placed quantum dots, increasing the length increases the chance that the transmission is limited by an extra ultra-small quantum dot within the nanoribbon [22, 23].

Figure 5(*c*) displays the relation of the energy gap E_g and the gap extension ΔV_{bg}. The energy gap E_g increases approximately linearly with ΔV_{bg}. The dashed line indicates the result of a linear fit. Even though the slope of the fit relates the back-gate voltage to an energy, it does not represent the lever arm of the back gate on the constriction, as the latter can be determined from Coulomb-blockade diamond measurements such as those shown in figure 3(*d*). The slope can rather be understood as describing the envelope of the diamond-shaped region of suppressed conductance that can, for example, be seen in figure 3(*b*). The constant of proportionality (linear slope) of E_g versus ΔV_{bg} suggests that the geometry of the constrictions has no major influence on the ratio of these two quantities. From a microscopic point of view, the linear relation between E_g and ΔV_{bg} is surprising. While the magnitude of the largest charging energy E_g is related to the length scale of the smallest quantum dot dominating the transmission through the constriction, the quantity ΔV_{bg} is related to the characteristic energy scale of the disorder potential [42]. The microscopic reason for the apparent relation between the length scale of the smallest dot in the constriction and the energy scale of the disorder potential remains an open question of graphene nanoribbon physics to date.

6. Conclusion

In conclusion, we have presented detailed transport measurements on graphene nanoribbons, focusing on the origin of the energy and transport gaps. We discuss a way to describe the transport gap by its width in back-gate voltage and compare it to the measurements of the conductance as a function of bias and back-gate voltages for different constriction geometries. Experimentally, we find two distinct energy scales characterizing these gaps. The first is the charging energy of local resonances or quantum dots forming along the ribbon. It depends on the size of the individual islands and corresponds to the extension of the region of suppressed conductance in the bias direction. The second is most probably dominated by the strength of the disorder potential, but also depends on the gap induced by confinement due to the ribbon boundaries. It is related to the extension of the gap in the back-gate direction. Finally, we discuss a transport model based on Coulomb blockade in nanoribbons giving rise to these two energy scales. However, the microscopic origin of their linear relation remains an open question. These insights are important to understand transport in graphene nanostructures and may significantly help in designing future graphene nanoelectronic devices.

Acknowledgments

The authors wish to thank A Castro-Neto, S Das Sarma, T Heinzel, S Hellmüller, M Hilke, F Libisch, K Todd, E Schurtenberger and L Vandersypen for helpful discussions. Support by the Swiss National Science Foundation and NCCR nanoscience is gratefully acknowledged.

References

[1] For review please see: Geim A K and Novoselov K S 2007 *Nat. Mater.* **6** 183
[2] Wang X, Ouyang Y, Li X, Wang H, Guo J and Dai H 2008 *Phys. Rev. Lett.* **100** 206803
[3] Zhang Q, Fang T, Xing H, Seabaugh A and Jena D 2008 *IEEE Electron Device Lett.* **29** 1344
[4] Meric I, Han M Y, Young A F, Oezyilmaz B, Kim P and Shepard K 2008 *Nature Nanotechnology* **3** 654
[5] Stampfer C, Güttinger J, Molitor F, Graf D, Ihn T and Ensslin K 2008 *Appl. Phys. Lett.* **92** 012102
[6] Ponomarenko L A, Schedin F, Katsnelson M I, Yang R, Hill E H, Novoselov K S and Geim A K 2008 *Science* **320** 356
[7] Stampfer C, Schurtenberger E, Molitor F, Güttinger J, Ihn T and Ensslin K 2008 *Nano Lett.* **8** 2378

[8] Schnez S, Molitor F, Stampfer C, Güttinger J, Shorubalko I, Ihn T and Ensslin K 2009 *Appl. Phys. Lett.* **94** 012107
[9] Molitor F, Dröscher S, Güttinger J, Jacobsen A, Stampfer C, Ihn T and Ensslin K 2009 *Appl. Phys. Lett.* **94** 222107
[10] Güttinger J, Stampfer C, Hellmüller S, Molitor F, Ihn T and Ensslin K 2008 *Appl. Phys. Lett.* **93** 212102
[11] Brey L and Fertig H A 2006 *Phys. Rev.* B **73** 235411
[12] White C T, Li J, Gunlycke D and Mintmire J W 2007 *Nano Lett.* **7** 825
[13] Wakabayashi K, Takane Y and Sigrist M 2007 *Phys. Rev. Lett.* **99** 036601
[14] Wakabayashi K, Takane Y, Yamamoto M and Sigrist M 2009 *Carbon* **47** 124
[15] Saito R, Dresselhaus G and Dresselhaus M S 1998 *Physical Properties of Carbon Nanotubes* (London: Imperial College Press)
[16] For review on carbon nanotubes see e.g. Reich S, Thomsen C and Maultzsch J 2003 *Carbon Nanotubes* (New York: Wiley-VCH)
[17] Son Y-W, Cohen M L and Louie S G 2006 *Nature* **444** 347
[18] Jiang J, Lu W and Bernholc J 2008 *Phys. Rev. Lett.* **101** 246803
[19] Chen Z, Lin Y-M, Rooks M and Avouris P 2007 *Physica* E **40** 228
[20] Han M Y, Özyilmaz B, Zhang Y and Kim P 2007 *Phys. Rev. Lett.* **98** 206805
[21] Todd K *et al* 2009 *Nano Lett.* **9** 416
[22] Stampfer C, Güttinger J, Hellmüller S, Molitor F, Ensslin K and Ihn T 2009 *Phys. Rev. Lett.* **102** 056403
[23] Molitor F, Jacobsen A, Stampfer C, Güttinger J, Ihn T and Ensslin K 2009 *Phys. Rev.* B **79** 075426
[24] Liu X *et al* 2009 arXiv:0812.4038
[25] Peres N M R, Casrtro Neto A H and Guinea F 2006 *Phys. Rev.* B **73** 195411
[26] Dunlycke D, Areshkin D A and White C T 2007 *Appl. Phys. Lett.* **90** 142104
[27] Fernandez-Rossier J, Palacios J J and Brey L 2007 *Phys. Rev.* B **75** 205441
[28] Yang L, Park C-H, Son Y-W, Cohen M L and Louie S G 2007 *Phys. Rev. Lett.* **99** 186801
[29] Lin Y-M, Perebeinos V, Chen Z and Avouris P 2008 arXiv:0805.0035v2
[30] Son Y-W, Cohen M L and Louie S G 2007 *Phys. Rev. Lett.* **99** 186801
[31] Mucciolo E R, Castro Neto A H and Lewenkopf C H 2008 arXiv:0806.3777v1
[32] Adam S, Cho S, Fuhrer M S and Sarma S Das 2008 *Phys. Rev. Lett.* **101** 046404
[33] Sols F, Guinea F and Neto A H Castro 2007 *Phys. Rev. Lett.* **99** 166803
[34] Evaldsson M, Zozoulenko I V, Hengyi Xu and Heinzel T 2008 *Phys. Rev.* B **78** 161407
[35] Novoselov K S, Geim A K, Morozov S V, Jiang D, Katsnelson M I, Dubonos S V, Grigorieva I V and Firsov A A 2004 *Science* **306** 666
[36] Novoselov K S, Geim A K, Morozov S V, Jiang D, Katsnelson M I, Grigorieva I V, Dubonos S V and Firsov A A 2005 *Nature* **438** 197–200
[37] Zhang Y, Tan Y-W, Stormer H L and Kim P 2005 *Nature* **438** 201–4
[38] Ferrari A C *et al* 2006 *Phys. Rev. Lett.* **97** 187401
[39] Graf D, Molitor F, Ensslin K, Stampfer C, Jungen A, Hierold C and Wirtz L 2007 *Nano Lett.* **7** 238
[40] Gupta A, Chen G, Joshi P, Tadigadapa S and Eklund P C 2006 *Nano Lett.* **6** 2667
[41] Molitor F, Güttinger J, Stampfer C, Graf D, Ihn T and Ensslin K 2007 *Phys. Rev.* B **76** 245426
[42] Martin J, Akerman N, Ulbricht G, Lohmann T, Smet J H, von Klitzing K and Yacoby A 2008 *Nature Phys.* **4** 144–8